Electronic structure and magnetic properties of magnetically dead layers in epitaxial $CoFe_2O_4/Al_2O_3/Si(111)$ films studied by x-ray magnetic circular dichroism

Yuki K. Wakabayashi,[1,*,†] Yosuke Nonaka,[2] Yukiharu Takeda,[3] Shoya Sakamoto,[2] Keisuke Ikeda,[2] Zhendong Chi,[2] Goro Shibata,[2] Arata Tanaka,[4] Yuji Saitoh,[3] Hiroshi Yamagami,[3,5] Masaaki Tanaka,[1,6] Atsushi Fujimori,[2] and Ryosho Nakane[1,7,‡]

[1]*Department of Electrical Engineering and Information Systems, The University of Tokyo, 7-3-1 Hongo, Bunkyo-ku, Tokyo 113-8656, Japan*
[2]*Department of Physics, The University of Tokyo, 7-3-1 Hongo, Bunkyo-ku, Tokyo 113-0033, Japan*
[3]*Materials Sciences Research Center, Japan Energy Atomic Agency, Sayo, Hyogo 679-5148, Japan*
[4]*Department of Quantum Matters, ADSM, Hiroshima University, Higashi-Hiroshima 739-8530, Japan*
[5]*Department of Physics, Kyoto Sangyo University, Motoyama, Kamigamo, Kita-Ku, Kyoto 603-8555, Japan*
[6]*Center for Spintronics Research Network, Graduate School of Engineering, The University of Tokyo, 7-3-1 Hongo, Bunkyo-ku, Tokyo 113-8656, Japan*
[7]*Institute for Innovation in International Engineering Education, The University of Tokyo, 7-3-1 Hongo, Bunkyo-ku, Tokyo 113-8656, Japan*

(Received 4 April 2017; revised manuscript received 22 July 2017; published 11 September 2017)

Epitaxial $CoFe_2O_4/Al_2O_3$ bilayers are expected to be highly efficient spin injectors into Si owing to the spin filter effect of $CoFe_2O_4$. To exploit the full potential of this system, understanding the microscopic origin of magnetically dead layers at the $CoFe_2O_4/Al_2O_3$ interface is necessary. In this paper, we study the cation distribution, electronic structures, and the magnetic properties of $CoFe_2O_4(111)$ layers with various thicknesses (thickness $d = 1.4$, 2.3, 4, and 11 nm) in the epitaxial $CoFe_2O_4(111)/Al_2O_3(111)/Si(111)$ structures using soft x-ray absorption spectroscopy (XAS) and x-ray magnetic circular dichroism (XMCD) combined with cluster-model calculation. The magnetization of $CoFe_2O_4$ measured by XMCD gradually decreases with decreasing thickness d, and finally, a magnetically dead layer is clearly detected at $d = 1.4$ nm. The magnetically dead layer has frustration of magnetic interactions, which is revealed from comparison between the magnetizations at 300 and 6 K. From analysis using configuration-interaction cluster-model calculation, the decrease of d leads to a decrease in the inverse-to-normal spinel structure ratio and also a decrease in the average valence of Fe at the octahedral sites. These results strongly indicate that the magnetically dead layer at the $CoFe_2O_4/Al_2O_3$ interface originates from various complex networks of superexchange interactions through the change in the cation distribution and electronic structure. Furthermore, from comparison of the magnetic properties between $d = 1.4$ and 2.3 nm, it is found that the ferrimagnetic order of the magnetically dead layer at the $CoFe_2O_4/Al_2O_3$ interface is partially restored by increasing the thickness from $d = 1.4$ to 2.3 nm.

DOI: 10.1103/PhysRevB.96.104410

I. INTRODUCTION

For the realization of Si-based spintronic devices, such as spin metal-oxide-semiconductor field-effect transistors (spin MOSFETs) [1–3], highly efficient spin injection into Si at room temperature is necessary. In a recent report [4], an epitaxial $CoFe_2O_4(111)/Al_2O_3(111)$ bilayer was grown on a Si (111) substrate. This structure has a potential ability of injecting a highly spin-polarized current into Si, since the ideal $CoFe_2O_4$ ferrimagnetic tunnel barrier is expected to exhibit the spin filter effect with 100% efficiency at room temperature, which is caused by the spin-dependent tunnel probability due to the oppositely spin-polarized lower and higher conduction bands of $CoFe_2O_4$ with inverse spinel structure, and $CoFe_2O_4$ has a Curie temperature T_C of 793 K which is high enough compared to room temperature [5–7]. Nevertheless, the experimental spin-polarization values estimated from tunnel magnetoresistance for $CoFe_2O_4$ tunnel barriers have been much less than the expectations [8,9], and many researchers point out the degradation of the electronic structure and magnetic properties of the $CoFe_2O_4$ films due to spontaneously formed structural disorder [6,10–14]. One recognized problem is that structural and chemical defects lead to the formation of midgap impurity states whose polarity is opposite to that of the lower conduction band of the inverse spinel structure [6,7,13]. Another problem is that antiphase boundaries (APBs) significantly reduce the magnetization of $CoFe_2O_4$, which becomes more pronounced with decreasing thickness [10–12]. However, these problems have not been studied on $CoFe_2O_4$ films which are thin enough for electron tunneling, i.e., a few nanometers thickness, probably because there is no established method that can clarify the structural disorder and electronic structure of such thin $CoFe_2O_4$ films. In general, it is plausible that magnetically dead layers formed at heterointerfaces degrade ferrimagnetic ordering of $CoFe_2O_4$ films with decreasing thickness; however, the magnetic properties of $CoFe_2O_4$ layers with various thicknesses have not been systematically investigated so far. Thus, it is vitally important to study the electronic structure and magnetic properties of the magnetically dead layers formed near the $CoFe_2O_4/Al_2O_3$ interface in epitaxial $CoFe_2O_4(111)/Al_2O_3(111)/Si(111)$ structures to achieve highly efficient spin injection into Si.

Soft x-ray absorption spectroscopy (XAS) and x-ray magnetic circular dichroism (XMCD) are extremely sensitive tools

*Present address: NTT Basic Research Laboratories, NTT Corporation, 3-1 Morinosato-Wakamiya, Atsugi, Kanagawa 243-0198, Japan.
†Corresponding author: wakabayashi.yuki@lab.ntt.co.jp
‡Corresponding author: nakane@cryst.t.u-tokyo.ac.jp

to the local electronic structure and magnetic properties of each element in magnetic thin films [15–19] and allow us to determine the crystallographic sites and valences of cations, which determine the physical properties of oxides [20–22]. In addition, because XMCD is free from the diamagnetic signal from the substrate, one can perform accurate measurements on ultrathin magnetically dead layers. Therefore, XMCD measurements are useful for the investigation of magnetically dead layers in oxide magnetic multilayers.

In this paper, we present the electronic structure and magnetic properties of $CoFe_2O_4(111)$ layers with various thicknesses (d) in epitaxial $CoFe_2O_4(111)/Al_2O_3(111)/Si(111)$ structures deduced using XAS and XMCD. The crystallographic sites and valences of the cations in the $CoFe_2O_4$ layers are determined using the experimental XMCD spectra and theoretical calculations based on the configuration-interaction (CI) cluster model [23]. We find that the magnetization gradually decreases with decreasing d from 11 to 4 nm and drastically decreases with decreasing d from 4 to 1.4 nm, and that the magnetization reduction is correlated to the change in the cation distribution and electronic structure. We also find that there is frustration of magnetic interactions in the magnetically dead layer. From these results, the magnetically dead layer at the $CoFe_2O_4/Al_2O_3$ interface probably originates from various complex networks of superexchange interactions through the change in the cation distribution and electronic structure. Furthermore, we also find that the ferrimagnetic order of the magnetically dead layer at the $CoFe_2O_4/Al_2O_3$ interface is partially restored by increasing the thickness from $d = 1.4$ to 2.3 nm.

II. SAMPLE FABRICATION AND CRYSTALLOGRAPHIC ANALYSES

Epitaxial $CoFe_2O_4(111)$ thin films with thickness $d = 1.4$, 2.3, 4, and 11 nm were grown on a 2.4-nm-thick γ-$Al_2O_3(111)$ buffer layer/n^+-Si(111) substrate using pulsed laser deposition (PLD). Figure 1 shows the schematic pictures of (a) the sample structure and (b) the spinel structure with the octahedral (O_h) and tetrahedral (T_d) sites. The small red, small blue, and large gray spheres in (b) represent the O_h sites, T_d sites, and oxygen anions, respectively. The blue and red arrows in (b) represent the antiferromagnetic coupling between the magnetic moment of the cations at the T_d and O_h sites. In the ideal inverse spinel structure, the T_d sites are only occupied by the Fe cations. The regularity of the cation distribution is represented by the inversion parameter y, which is an inverse-to-normal spinel structure ratio defined by the chemical formula $[Co_{1-y}Fe_y]_{Td}[Fe_{2-y}Co_y]_{Oh}O_4$. Our detailed fabrication technique and characterizations are as follows.

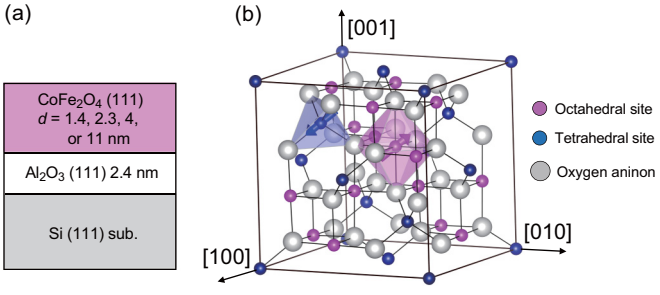

FIG. 1. Schematic pictures of (a) the sample structure and (b) the spinel structure with the octahedral (O_h) and tetrahedral (T_d) sites. The small red, small blue, and large gray spheres in (b) represent the O_h sites, T_d sites, and oxygen anions, respectively. The blue and red arrows in (b) represent the antiferromagnetic coupling between the magnetic moment of the cations at the T_d and O_h sites.

Highly phosphorus-doped Si(111) wafers with the low resistivity of 2 mΩ cm were used as substrates to avoid charging of samples [24] during XAS and XMCD measurements. For the growth of epitaxial γ-Al_2O_3 buffer layers just on the Si surfaces, we used solid-phase reaction of Al and SiO_2. The procedure is basically the same as that used in Ref. [25]. A Nd : YAG laser used for the PLD method was operated under the following conditions: wavelength 266 nm (fourfold wave), pulse duration 10 nsec, and pulse repetition rate 10 Hz.

First, a Si substrate was chemically cleaned with the Radio Corporation of America (RCA) method, followed by hydrogen fluoride (HF) dip. Then the hydrogen-terminated surface of the Si substrate was oxidized at 80 °C for 5 min in a $HCl : H_2O_2 : H_2O = 3 : 1 : 1$ solution to form a thin SiO_2 layer. Subsequently, the substrate was installed into an ultrahigh vacuum deposition system having a molecular beam epitaxy (MBE) chamber and a PLD chamber. After the thermal cleaning at substrate temperature (T_{SUB}) = 200 °C for 30 min, T_{SUB} was lowered to room temperature, and then a 0.6-nm-thick Al layer was deposited on the thin SiO_2 surface using a Knudsen cell in the MBE chamber. After that, the substrate was transferred to the PLD chamber via a vacuum transport chamber, and a γ-Al_2O_3 buffer layer was formed by solid-phase reaction of Al and SiO_2 at $T_{SUB} = 820$ °C for 30 min with the base pressure below 5.0×10^{-7} Pa. As seen in Figs. 2(a) and 2(b), reflective high-energy electron diffraction (RHEED) patterns showed the Si substrate streaks together with sixfold streaks indicating epitaxial γ-Al_2O_3, which were completely the same patterns as those in Ref. [25]. To obtain a more ordered surface, a 1-nm-thick epitaxial γ-Al_2O_3 layer was subsequently grown using a single-crystalline Al_2O_3 target with a rate of 0.2 nm/min under a O_2 pressure (P_{O2}) of 1×10^{-4} Pa. After the growth, the Si substrate streaks vanished, and the sixfold γ-Al_2O_3 streaks became more intense and showed a 1×2 reconstruction pattern, as shown in Figs. 2(c) and 2(d). Then T_{SUB} was lowered to 500 °C with a rate of 30 °C/ min under $P_{O2} = 1 \times 10^{-4}$ Pa, and finally, an epitaxial $CoFe_2O_4$ layer was grown using a sintered $CoFe_2O_4$ target with a deposition rate of 0.12 nm/min. To obtain a high crystallinity, $P_{O2} = 10$ Pa was used for this growth. Figures 2(e) and 2(f) show RHEED patterns of an 11-nm-thick $CoFe_2O_4$ layer, in which very sharp streaks with a 2×2 reconstruction and higher-order Laue patterns can be clearly seen. This indicates a high-quality two-dimensional epitaxial growth mode of the $CoFe_2O_4$ layer. The sixfold symmetry with the 2×2 reconstruction was also confirmed by a low-energy electron diffraction (LEED) pattern (see Fig. S1 in Sec. I of the Supplemental Material [26]). We observed almost the same RHEED and LEED patterns for epitaxial $CoFe_2O_4$ layers with various thicknesses ($d = 1.4$, 2.3, and 4 nm). From the analysis of the RHEED patterns, the in-plane lattice constant of the γ-Al_2O_3 layer was smaller by $\sim 2\%$ than that of bulk γ-Al_2O_3, which is probably due to the lattice mismatch $\sim 2\%$

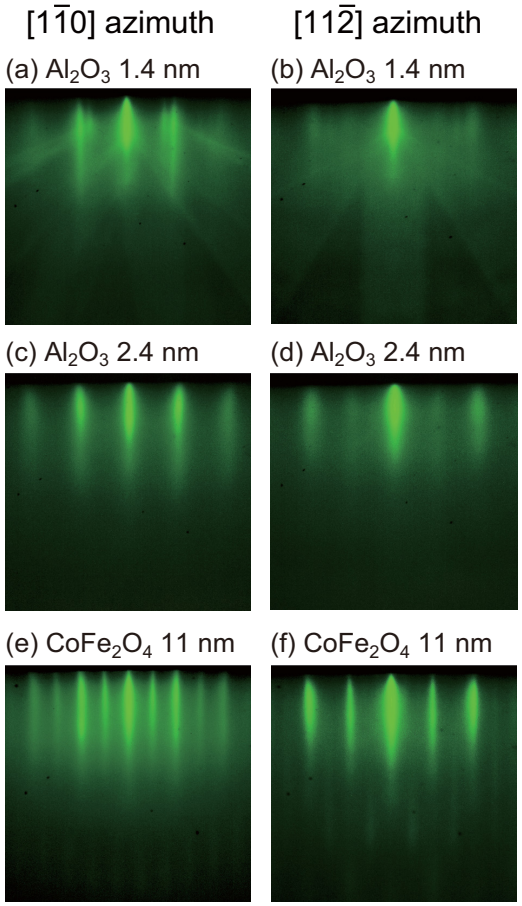

FIG. 2. RHEED patterns of an epitaxial $CoFe_2O_4$/γ-Al_2O_3(111)/Si(111) structure, where the electron incidences are along the (a), (c), and (e) [1$\bar{1}$0] and (b), (d), and (f) [11$\bar{2}$] directions of the Si substrate. (a) and (b) After the growth of 1.4-nm-thick γ-Al_2O_3(111) on the Si surface by annealing. (c) and (d) After the growth of an additional 1-nm-thick γ-Al_2O_3 layer by PLD. (e) and (f) After the growth of an 11-nm-thick $CoFe_2O_4$ layer by PLD.

with respect to Si, whereas the in-plane lattice constant of the $CoFe_2O_4$ layer was smaller by $\sim 1\%$ than that of bulk $CoFe_2O_4$. Thus, both layers were compressively strained in the film plane.

We evaluated the surface roughness by atomic force microscopy (AFM) and found that the surfaces of the grown γ-Al_2O_3 layer and the $CoFe_2O_4$ layers are continuous and very smooth, as shown in Figs. 3(a) and 3(b): Root mean square (RMS) values for the γ-Al_2O_3 layer and $CoFe_2O_4$ layers were typically 0.25 and 0.28 nm, respectively. In Fig. 3(b), one can see facets of islands which reflect the crystallographic directions of the $CoFe_2O_4$ layer. Note that the RMS values of the epitaxial $CoFe_2O_4$ layers with various thicknesses ($d = 1.4$, 2.3, 4, and 11 nm) were almost the same, i.e., there is no thickness dependence.

Next, we characterized the crystallographic properties by x-ray diffraction (XRD). For the estimation of the out-of-plane lattice constant, the θ-2θ method was used (see Fig. S2 in Sec. I of the Supplemental Material [26]). The out-of-plane lattice constant of the γ-Al_2O_3 layer was larger by 6% than that of the bulk, and therefore, bulk γ-Al_2O_3 layer was

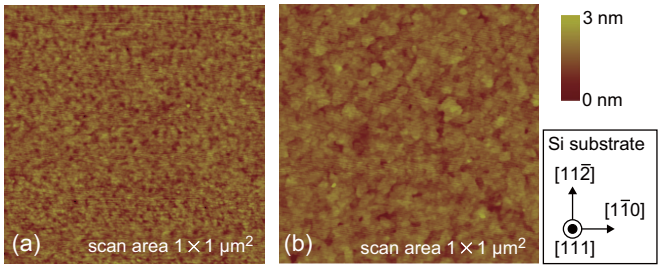

FIG. 3. AFM images of (a) the 2.4-nm-thick γ-Al_2O_3(111) layer and (b) the 11-nm-thick $CoFe_2O_4$ layer in an epitaxial $CoFe_2O_4$/γ-Al_2O_3(111)/Si(111) structure. The scan area is $1 \times 1\ \mu m^2$. The crystallographic directions of the Si substrate are also shown.

tensile strained. On the other hand, the out-of-plane lattice constant of bulk $CoFe_2O_4$ layer was the same as that of the bulk. As expected from the RHEED and LEED patterns, the sixfold symmetry of γ-Al_2O_3 and $CoFe_2O_4$ layers were observed by the ϕ scan XRD patterns for γ-Al_2O_3(311) and $CoFe_2O_4$(311) (see Fig. S3 in Sec. I of the Supplemental Material [26]), which indicates that one domain completely aligns to the Si substrate with the epitaxial relationship of γ-Al_2O_3[11$\bar{2}$](111)//$CoFe_2O_4$[11$\bar{2}$](111)//Si[11$\bar{2}$](111), whereas another domain is rotated by 60° in the (111) plane. This double domain structure is basically the same as that in Ref. [4].

Figures 4(a) and 4(b) show the cross-sectional high-resolution transmission electron microscopy (HRTEM) images of the $CoFe_2O_4$ film with $d = 11$ nm projected along the Si ⟨11$\bar{2}$⟩ axis. Almost the entire region of the $CoFe_2O_4$ layer has an epitaxially grown single-crystalline structure with a

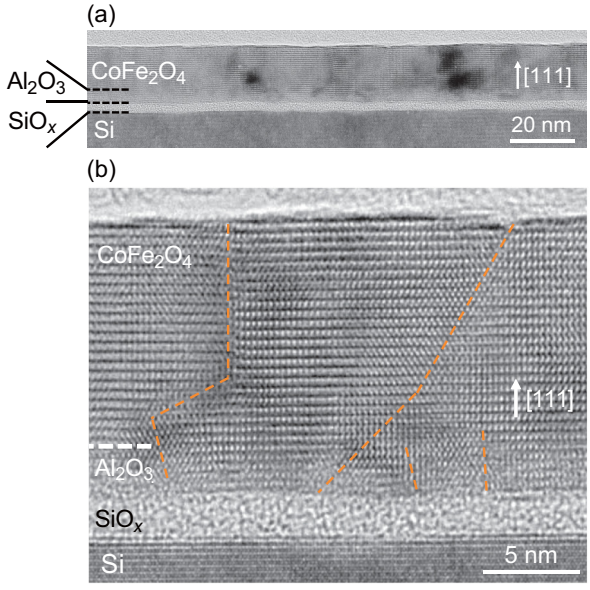

FIG. 4. (a) HRTEM lattice image of the $CoFe_2O_4$ film with $d = 11$ nm projected along the Si ⟨11$\bar{2}$⟩ axis. (b) Magnified image of (a). The orange dashed lines represent APBs. The oxygen lattice remains unchanged across the APB while the cation sublattice shifts by a ⟨220⟩ translation vector.

smooth and flat surface and interface with the γ-Al_2O_3 buffer layer, as expected from the RHEED patterns, the AFM images, and the XRD analysis. One can observe a ∼2.1-nm-thick SiO_x interfacial layer, which might be caused by the high O_2 pressure of 10 Pa during the growth of the $CoFe_2O_4$ layer. The orange dashed lines represent APBs, which are growth defects of the cation sublattice in the spinel structure [10–12]: The oxygen lattice remains unchanged across an APB whereas the cation sublattice is shifted by the ⟨220⟩ translation vector [12]. In the previous reports on $CoFe_2O_4$/MgO [27] and $CoFe_2O_4$/α-Al_2O_3 [12], the density of APBs decreases with increasing thickness of the $CoFe_2O_4$ layer since APBs, which are mainly introduced at the heterointerface, vanish monotonically with increasing thickness. Contrary to these, in our case, the heterointerface $CoFe_2O_4$/γ-Al_2O_3 is not clearly identified in Fig. 4(b), and thus, it is not the main source of APBs. As seen in Fig. 4(b), two APBs penetrate the whole $CoFe_2O_4$ layers, and the other two APBs vanish in the γ-Al_2O_3 buffer layer. Since the APB distribution is basically the same in a wide area, it seems that the density of APBs does not depend on the thickness of the $CoFe_2O_4$ layer.

III. XAS AND XMCD MEASUREMENTS

We performed XAS and XMCD measurements at the soft x-ray beamline BL23SU of SPring-8 with a twin-helical undulator of in-vacuum type [28], which allows us to perform efficient and accurate measurements of XMCD with various incident photon energies and magnetic fields. The monochromator resolution was $E/\Delta E > 10\,000$. X-ray magnetic circular dichromism spectra were obtained by reversing the photon helicity at each energy point and were recorded in the total-electron-yield (TEY) mode. It is well recognized that XAS and XMCD signals measured in the TEY mode originate from magnetic ions located within the depth of 2–3 nm from the film surface [29]. To eliminate experimental artifacts, we averaged XMCD spectra taken for both positive and negative magnetic fields applied perpendicular to the film surface. The direction of the incident x-rays was also perpendicular to the film surface. Backgrounds of the XAS spectra at the Fe and Co $L_{2,3}$ edges were subtracted from the raw data, assuming that they are hyperbolic tangent functions.

Figure 5 shows the Fe and Co $L_{2,3}$ edge XAS [μ^-, μ^+, and $(\mu^+ + \mu^-)/2$] and XMCD ($\mu^+ - \mu^-$) spectra for the $CoFe_2O_4$ film with $d = 11$ nm measured at 6 and 300 K with magnetic fields $\mu_0 H = 0$, 1, and 7 T. The spectra with both $\mu_0 H = 0$ and 1 T were measured after the application of $\mu_0 H = 7$ T. Here, μ^+ and μ^- denote the absorption coefficients for the photon helicities parallel and antiparallel to the Co 3d majority spin direction, respectively. These spectra show the multiplet structures which are a characteristic of the localized 3d state of Fe and Co cations in oxides [20–22]. For both the Fe and Co $L_{2,3}$ edges, the XMCD spectra with $\mu_0 H = 7$ T are identical between 6 and 300 K, indicating that the T_C of the $CoFe_2O_4$ film is sufficiently higher than 300 K. The XMCD intensities with $\mu_0 H = 0$ T originate from the remanent-spontaneous magnetization. The insets of Figs. 5(c) and 5(d) show the magnified plots of the XMCD spectra at the L_3 edges normalized at 709.2 and 778.2 eV, respectively. For both the Fe and Co L_3 edges, the normalized XMCD spectra for various H are identical with each other, indicating that the XMCD signals come from a single magnetic phase. Since the same features were also observed for the $CoFe_2O_4$ films with $d = 1.4$, 2.3, and 4 nm (see Sec. II of the Supplemental Material [26]), all the $CoFe_2O_4$ films with various thicknesses are magnetically uniform. The Fe L_3 edge XMCD spectrum has two negative peaks at 707.38 (peak a) and 709.18 eV (peak c) and a positive peak at 708.48 eV (peak b). It is well known that the XMCD peaks at a, b, and c mainly come from Fe cations at Fe^{2+} (O_h), Fe^{3+} (T_d), and Fe^{3+} (O_h) sites,

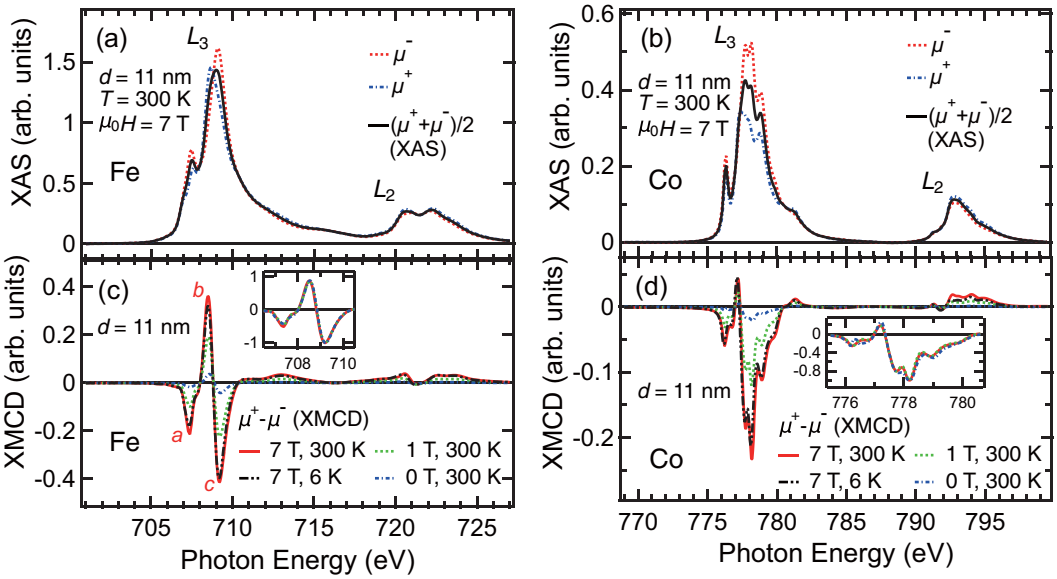

FIG. 5. (a) Fe and (b) Co $L_{2,3}$ edge XAS [$(\mu^+ + \mu^-)/2$] spectra for the $CoFe_2O_4$ film with $d = 11$ nm measured at 300 K with a magnetic field $\mu_0 H = 7$ T applied perpendicular to the film surface. (c) Fe and (d) Co $L_{2,3}$ edge XMCD ($= \mu^+ - \mu^-$) spectra for the $CoFe_2O_4$ film with $d = 11$ nm measured at 6 and 300 K with magnetic fields $\mu_0 H = 0$, 1, and 7 T applied perpendicular to the film surface. The insets of (c) and (d) show magnified plots of the spectra at the L_3 edges normalized at 709.2 and 778.2 eV, respectively.

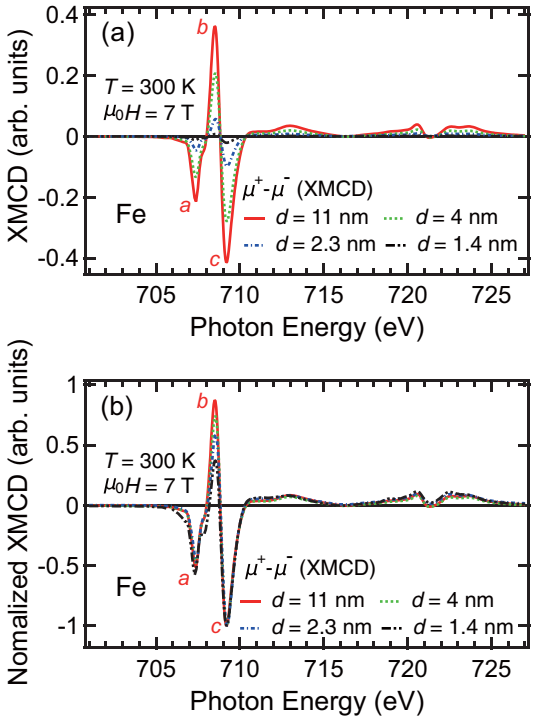

FIG. 6. (a) Fe $L_{2,3}$ edge XMCD spectra for the $CoFe_2O_4$ films with $d = 1.4$, 2.3, 4, and 11 nm measured at 300 K with a magnetic field $\mu_0 H = 7$ T applied perpendicular to the film surface. (b) Spectra in (a) normalized to the intensity at 709.2 eV.

respectively [20,30], where the superscript number denotes the valence of the Fe cations. Our calculation also supports these assignments, as we shall show below [Figs. 7(a) and 7(b)]. The comparable peak height of peak b and peak c indicates that the amount of the Fe^{3+} (T_d) cations is comparable to that of the Fe^{3+} (O_h) cations. This result means that the $CoFe_2O_4$ layer has a high inversion parameter y. On the other hand, the XMCD signals at the Co L_3 edge are mostly negative. Thus, it was found that the magnetic moments of the Fe^{3+} (T_d) cations and Co cations have an antiparallel configuration, as shown in Fig. 1(b), which is a characteristic feature of the Co (O_h) cations in inverse spinel ferrites [20].

Figure 6(a) shows the Fe $L_{2,3}$ edge XMCD spectra for the $CoFe_2O_4$ films with $d = 1.4$, 2.3, 4, and 11 nm, which were measured at 300 K with $\mu_0 H = 7$ T. The maximum XMCD intensity at the Fe L_3 edge decreases by 33% in going from 11 to 4 nm, and then it drastically decreases by 79% in going from 4 to 1.4 nm. The normalized XMCD intensity at the peak b, which comes from the Fe^{3+} (T_d) cations, decreases with decreasing d [Fig. 6(b)]. Thus, the drastic reduction of the magnetization is seemingly associated with the decrease in the inverse-to-normal spinel structure ratio.

To clarify the correlation between the magnetization, the cation distribution, and electronic structure quantitatively, we analyzed the crystallographic sites and valences of Fe and Co cations using the experimental XMCD spectra and cluster-model calculation. It has been well recognized that the XAS and XMCD spectra of transition-metal oxides strongly depend on the $3d$ electron configurations, crystal field, spin-orbit coupling, and electron-electron interaction within the transition-metal cation, and the hybridization of $3d$ electrons with other valence electrons. Taking into account these effects, XAS and XMCD spectra for Fe and Co with a specific site and valence can be calculated by employing the CI cluster model [23]. In the cluster-model calculation, we adopted empirical relationships between the onsite Coulomb energy U_{dd} and the $3d$-$2p$ hole Coulomb energy U_{dc} : $U_{dc}/U_{dd} = 1.25$ [30], and between the Slater-Koster parameters $pd\sigma$ and $pd\pi$: $pd\sigma/pd\pi = -2.17$ [31]. The hybridization strength between O $2p$ orbitals T_{pp} was fixed to be 0.7 eV (for O_h site) and 0 eV (for T_d site) [23,30]. The 80% of ionic Hartree-Fock values were used for Slater integrals. In the cluster-model calculation for Fe cations, model parameters were determined as follows: We used the reported Fe_3O_4 values of the U_{dd} [30]. Charge-transfer energy Δ, which is defined as the energy required to transfer an electron from O $2p$ to Fe $3d$ orbitals, the crystal field splitting $10Dq$, and the Slater-Koster parameters $pd\sigma$ between Fe $3d$ and O $2p$ were determined by curve fitting to the experimental Fe $L_{2,3}$ edge XAS and XMCD spectra (particularly for the L_3 edges) measured at 300 K with $\mu_0 H = 7$ T of the $CoFe_2O_4$ film with $d = 11$ nm. The parameter values determined for the Fe cations are listed in Table I.

TABLE I. Parameter values (in units of eV) used in the calculation based on the CI cluster model. For the Fe cations, U_{dd} was adopted from [30].

	Δ	$10Dq$	$pd\sigma$	U_{dd}
Fe^{3+} (O_h)	0.4	0.9	1.2	6.0
Fe^{3+} (T_d)	4.0	−0.5	2.0	6.0
Fe^{2+} (O_h)	6.5	0.9	1.6	6.0
Co^{2+} (O_h)	5.6	0.5	1.3	6.5
Co^{2+} (T_d)	6	−0.3	1.4	6.0
Co^{3+} (O_h)	0	0.5	1.3	6.0

Figures 7(a) and 7(b) show the calculated Fe $L_{2,3}$ edge XAS and XMCD spectra for the Fe^{3+} (O_h), Fe^{3+} (T_d), and Fe^{2+} (O_h) cations, respectively, using the parameters in Table I. The spin magnetic moment m_{spin} and the orbital magnetic moment m_{orb} were also calculated within the CI cluster model based on the above parameters for the Fe^{3+} (O_h), Fe^{3+} (T_d), and Fe^{2+} (O_h) cations, and these are summarized in Table II. Figures 7(c) and 7(d) show the experimental Fe $L_{2,3}$ edge XAS and XMCD spectra measured at 300 K with $\mu_0 H = 7$ T for the $CoFe_2O_4$ films with $d = 1.4$, 2.3, 4, and 11 nm, and the corresponding curve fittings (particularly for the L_3 edges) with the weighted sum of the calculated spectra shown in Figs. 7(a) and 7(b). The experimental spectra are well reproduced by the weighted sum of the calculated spectra, including the characteristic kink structure at around 708 eV in the experimental XMCD spectra. These results give a strong evidence that the Fe cations only occupy the Fe^{3+} (O_h), Fe^{3+} (T_d), and Fe^{2+} (O_h) sites. From these fits, we can obtain the magnetic moment of the Fe^{3+} (O_h), Fe^{3+} (T_d), and Fe^{2+} (O_h) cations at 300 K with $\mu_0 H = 7$ T and the site occupancies for the Fe cations.

Figure 8(a) shows the d dependence of the site occupancies for Fe^{3+} (O_h), Fe^{3+} (T_d), and Fe^{2+} (O_h) estimated from the same fitting procedure. In the figure, the inversion parameter y is also shown. The y value gradually decreases with decreasing

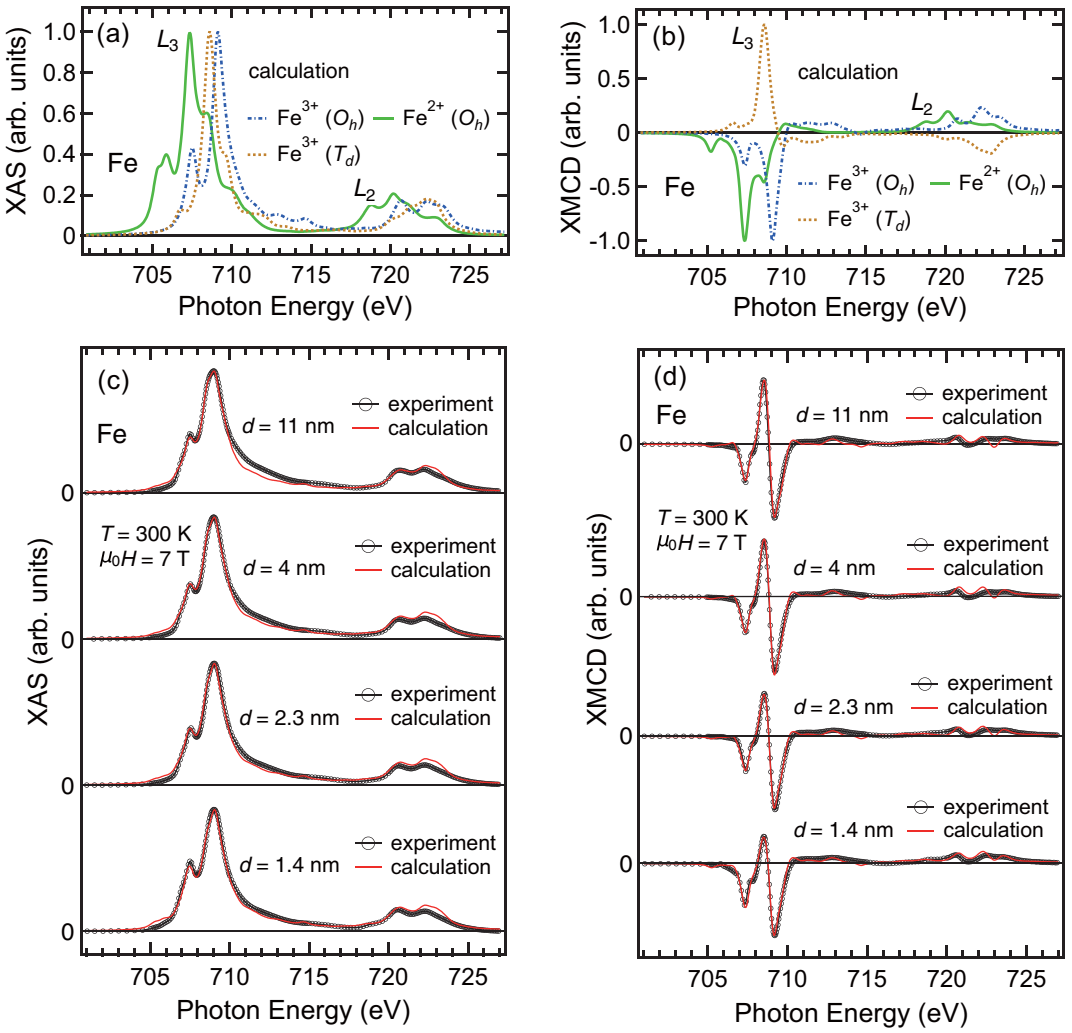

FIG. 7. Calculated Fe $L_{2,3}$ edge (a) XAS and (b) XMCD spectra, where the dot-dashed, dotted, and solid curves represent the spectra for Fe^{3+} (O_h), Fe^{3+} (T_d), and Fe^{2+} (O_h), respectively. Experimental Fe $L_{2,3}$ edge (c) XAS and (d) XMCD spectra for the $CoFe_2O_4$ films with d = 1.4, 2.3, 4, and 11 nm measured at 300 K with a magnetic field $\mu_0 H = 7$ T applied perpendicular to the film surface. In the figure, the circles are experimental data, and the red curves are the weighted sum of the calculated spectra shown in panels (a) and (b). Each spectrum has been arbitrarily scaled for easy comparison.

d and finally drops to 0.54 at $d = 1.4$ nm. Another striking feature is that the site occupancy for Fe^{2+} (O_h) at $d = 1.4$ nm is twice as large as those in the thicker samples, whereas the site occupancy for Fe^{3+} (O_h) is almost independent of d. Thus, the decrease of d leads to the decrease in the inverse-to-normal spinel structure ratio and also the decrease in the average valence of the Fe cations at the O_h sites.

In the calculation for the Co cations using the CI cluster model, the parameters were determined as follows: The Δ, $10Dq$, U_{dd}, and $pd\sigma$ were determined by the curve fitting for the experimental Co $L_{2,3}$ edge XAS and XMCD spectra measured at 300 K with $\mu_0 H = 7$ T of the $CoFe_2O_4$ film with $d = 11$ nm. The determined parameter values for the Co cations are also listed in Table I.

Figures 9(a) and 9(b) show the calculated Co $L_{2,3}$ edge XAS and XMCD spectra for the Co^{2+} (O_h), Co^{2+} (T_d), and Co^{3+} (O_h) cations, respectively, using the parameters in Table I. The spin magnetic moment m_{spin} and the orbital magnetic moment m_{orb} were also calculated within the cluster model using the above parameters for the Co^{2+} (O_h), Co^{2+}

TABLE II. m_{spin} and m_{orb} (μ_B/atom) calculated within the CI cluster model for the Fe^{3+} (O_h), Fe^{3+} (T_d), Fe^{2+} (O_h), Co^{2+} (O_h), Co^{2+} (T_d), and Co^{3+} (O_h) cations.

	Fe^{3+} (O_h)	Fe^{3+} (T_d)	Fe^{2+} (O_h)	Co^{2+} (O_h)	Co^{2+} (T_d)	Co^{3+} (O_h)
m_{spin} (μ_B/atom)	4.406	4.557	3.620	2.54	2.87	3.20
m_{orb} (μ_B/atom)	0.015	0.004	0.556	1.07	0.47	0.70

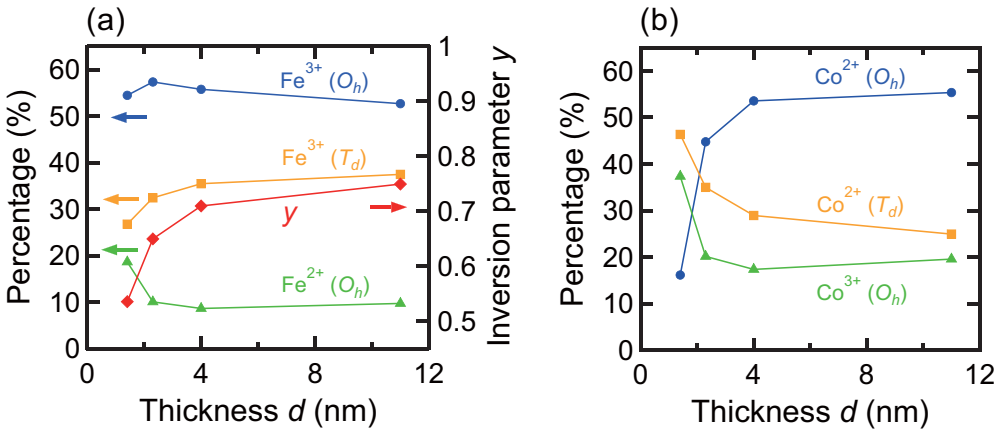

FIG. 8. (a) Thickness d dependence of the site occupancies for the Fe cations, where the circles, squares, and triangles represent Fe^{3+} (O_h), Fe^{3+} (T_d), and Fe^{2+} (O_h), respectively. Inversion parameter y is also shown as rhombuses. (b) Thickness d dependence of the site occupancies for the Co cations, where the circles, squares, and triangles represent Co^{2+} (O_h), Co^{2+} (T_d), and Co^{3+} (O_h), respectively. Here, the site occupancies for the Co cations are calculated from those for the Fe cations shown in (a) so that the charge neutrality is fulfilled, and the number ratio of the O_h sites to the T_d sites is 2 in the $CoFe_2O_4$ layer.

(T_d), and Co^{3+} (O_h) cations, and these are also summarized in Table II. Figures 9(c) and 9(d) show the experimental Co $L_{2,3}$ edge XAS and XMCD spectra measured at 300 K with $\mu_0 H = 7$ T for the $CoFe_2O_4$ films with $d = 1.4$, 2.3, 4, and 11 nm, and the weighted sum of the calculated spectra shown in Figs. 9(a) and 9(b). Here, the site occupancies for the Co cations shown in Fig. 8(b) were calculated from those for the Fe cations shown in Fig. 8(a) so that the charge neutrality is fulfilled and the number ratio of the O_h sites to the T_d sites is 2 in the $CoFe_2O_4$ layer. From these calculations, we obtain the magnetization of the Co^{2+} (O_h), Co^{2+} (T_d), and Co^{3+} (O_h) cations at 300 K with $\mu_0 H = 7$ T. The experimental XAS and XMCD spectra with $d = 11$ nm are well reproduced by the weighted sum of the calculated spectra as shown in Figs. 9(c) and 9(d), which indicates that most Co cations occupy the Co^{2+} (O_h), Co^{2+} (T_d), and Co^{3+} (O_h) sites in the $CoFe_2O_4$ film with $d = 11$ nm. However, the discrepancy between the experimental spectra and the weighted sum of the calculated spectra increases with decreasing d, and finally, the experimental XMCD spectra with $d = 1.4$ nm cannot be reproduced by the weighted sum of the calculated spectra [Fig. 9(d)], although each calculated spectrum is the best fit after investigating a vast amount of parameter values/sets. This suggests that factors other than the assumptions in the calculation become more significant with decreasing d; some other Co cations, such as low spin Co cations [32], Co cations at the trigonal prism sites [33], and Co cations under local distortion, and/or a different ratio of the O_h site to the T_d site [34]. This leads to a consideration that such structural and chemical defects were introduced at the $CoFe_2O_4/Al_2O_3$ interface, and they disappear gradually with increasing d. This is partly similar to the result of a Fe_3O_4 film deposited on a MgO substrate in Ref. [34], in which the T_d site is completely missing at the Fe_3O_4/MgO interface and the ratio of the O_h site to the T_d site approaches 2 as the thickness of the Fe_3O_4 film increases.

Figures 10(a)–10(d) show the XMCD H curves at the Fe L_3 edge for the $CoFe_2O_4$ films with $d = 11$, 4, 2.3, and 1.4 nm, respectively, in which red curves and blue curve are the results measured at 300 and 6 K, respectively. Here, we have scaled the vertical axis so that the XMCD intensity at 300 K with $\mu_0 H = 7$ T represents the sum of the magnetizations of the Fe and Co cations. Taking into account the antiferromagnetic coupling between the magnetic moment of the cations at T_d and O_h sites, the sum of the magnetizations was calculated from the sum of the magnetic moments of the Fe^{3+} (O_h), Fe^{3+} (T_d), Fe^{2+} (O_h), Co^{2+} (O_h), Co^{2+} (T_d), and Co^{3+} (O_h) cations estimated in Figs. 7(c), 7(d), 9(c), and 9(d) with the ratio of the site occupancies shown in Fig. 8. In all the samples, the normalized XMCD-H curves measured at various energies at the Fe and Co L_3 edges are identical, which confirms again that the XMCD signals come from a single magnetic component (see Sec. III of the Supplemental Material [26]). One can clearly see hysteresis in the $CoFe_2O_4$ film with $d = 11$ nm, which indicates that T_C is higher than 300 K. For $d \leqslant 4$ nm, the XMCD-H curve at 300 K does not have hysteresis, its linearity increases with decreasing d, and finally, it shows a nearly straight line for $d = 1.4$ nm. These features indicate that random magnetization configurations in zero field [11,27] are induced by various complex networks of superexchange interactions through the change in the cation distribution and electronic structures shown in Fig. 8. As described in Sec. III, the present XMCD signals measured in the TEY mode originate from magnetic ions located within the depth of 2–3 nm from the surface [29]. To confirm this, we plotted the maximum XAS intensity at the Fe L_3 edge as a function of d and found that, as d increases, it increases in the range of $d = 1.4$ to 2.3 nm, and then it saturates above $d = 2.3$ nm (see Fig. S8 in Sec. IV of the Supplemental Material [26]). This result means that the XMCD signals for $d = 1.4$ and 2.3 nm reflect the magnetic properties at the $CoFe_2O_4/Al_2O_3$ interface, whereas those for $d = 4$ and 11 nm do not. Thus, the nearly linear XMCD-H relation for $d = 1.4$ nm at 300 K probably come from a magnetically dead layer formed at the $CoFe_2O_4/Al_2O_3$ interface. To study this further, XMCD-H for $d = 1.4$ nm was also measured at 6 K, as shown by a blue curve in Fig. 10(d). Although the curve is slightly nonlinear,

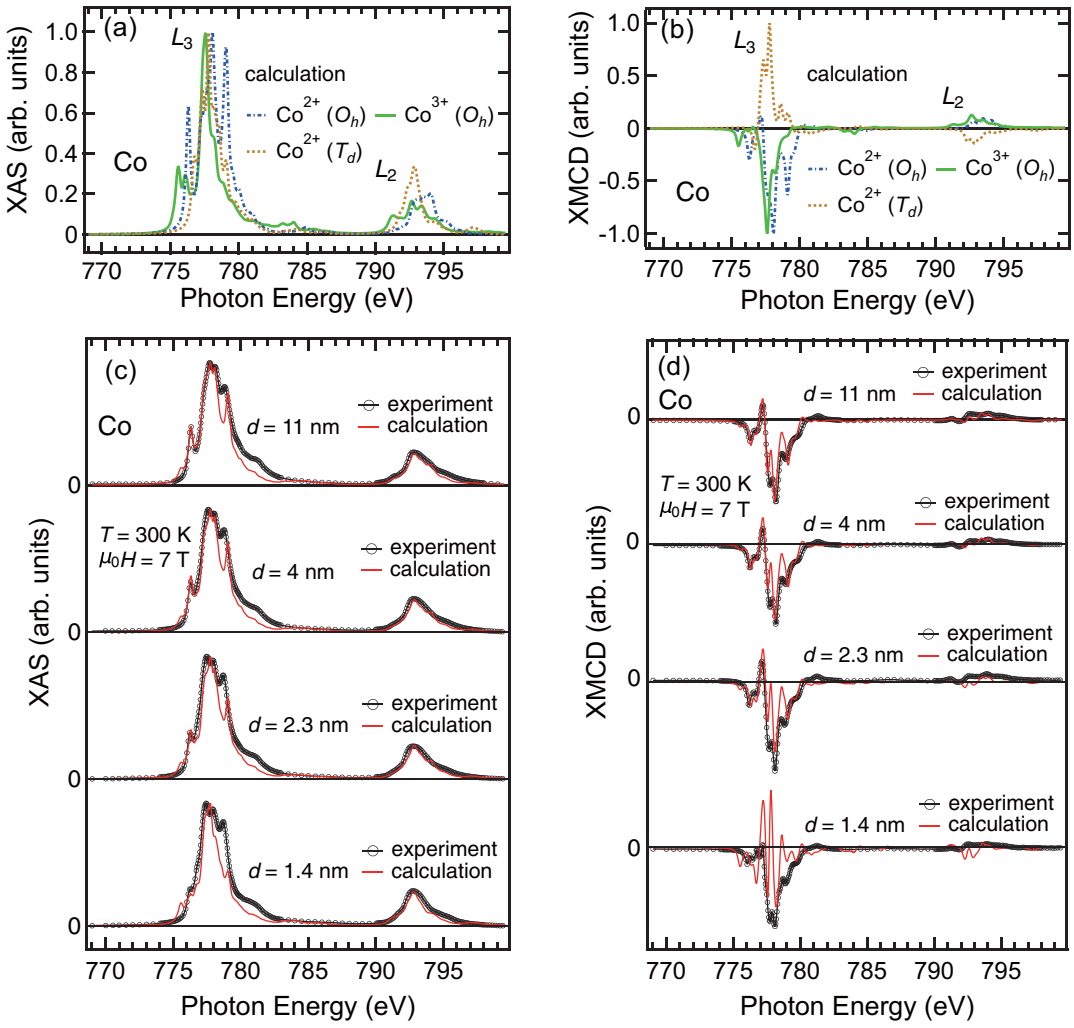

FIG. 9. Calculated Co $L_{2,3}$ edge (a) XAS and (b) XMCD spectra, where the dot-dashed, dotted, and solid curves represent Co^{2+} (O_h), Co^{2+} (T_d), and Co^{3+} (O_h), respectively. Experimental Co $L_{2,3}$ edge (c) XAS and (d) XMCD spectra for the $CoFe_2O_4$ films with d = 1.4, 2.3, 4, and 11 nm measured at 300 K with a magnetic field $\mu_0 H = 7$ T applied perpendicular to the film surface. In the figures, the circles are experimental data, and the red curves are the weighted sum of the calculated spectra shown in panels (a) and (b). Here, the site occupancies for the Co cations are estimated from that for the Fe cations shown in Fig. 8 under the conditions that the charge neutrality is maintained and that the number ratio of the O_h sites to the T_d sites is 2. Each spectrum has been arbitrarily scaled for easy comparison.

the magnetization at 7 T was increased by only 2.5 times when temperature was decreased from 300 to 6 K, which means that the magnetization does not originate only from paramagnetic component and that there is frustration of magnetic interactions induced by various complex networks of superexchange interactions in the magnetically dead layer. On the other hand, the XMCD-H curve for $d = 2.3$ nm is less linear than that for $d = 1.4$ nm. Since all the XMCD signals come from the single magnetic phase as described above, the ferrimagnetic order of the magnetically dead layer at the $CoFe_2O_4/Al_2O_3$ interface is partially restored by increasing the thickness from $d = 1.4$ to 2.3 nm. This restoration of the ferrimagnetic order of the magnetically dead layer at $d = 1.4$ nm likely originates from an interlayer coupling with the additional 0.9-nm-thick $CoFe_2O_4$ layer having a stronger ferrimagnetic ordering since the regularity of the cation distribution becomes higher with increasing d. Thus, the magnetic properties of the magnetically dead layer at the $CoFe_2O_4/Al_2O_3$ interface are found to be determined not only by the cation distribution and electronic structure near the interface, but also by the thickness of the $CoFe_2O_4$ layer.

In the following, we discuss our results in comparison with previous studies by other groups. To our knowledge, it is well recognized that APBs, which are growth defects in the cation sublattice, induce 180° Fe-O-Fe antiferromagnetic superexchange interactions and reduce the magnetization of magnetite Fe_3O_4 films [10,11]. Moussy *et al.* [12] reported that the density of APBs in epitaxial Fe_3O_4(111) films increased with decreasing thickness, and this feature led to the decrease of the magnetization with decreasing thickness; the magnetization at 300 K with $\mu_0 H = 1$ T decreased by ∼15% with decreasing thickness from 15 to 5 nm. In our case, as shown in Fig. 11, the sum of the magnetizations of the Fe and Co cations in the $CoFe_2O_4$ film at 7 T decreased by 43% from $d = 11$ to 4 nm. Thus, the decrease ratio of the magnetization in the $CoFe_2O_4$ films in the large thickness range (11 to 4 nm) is slightly

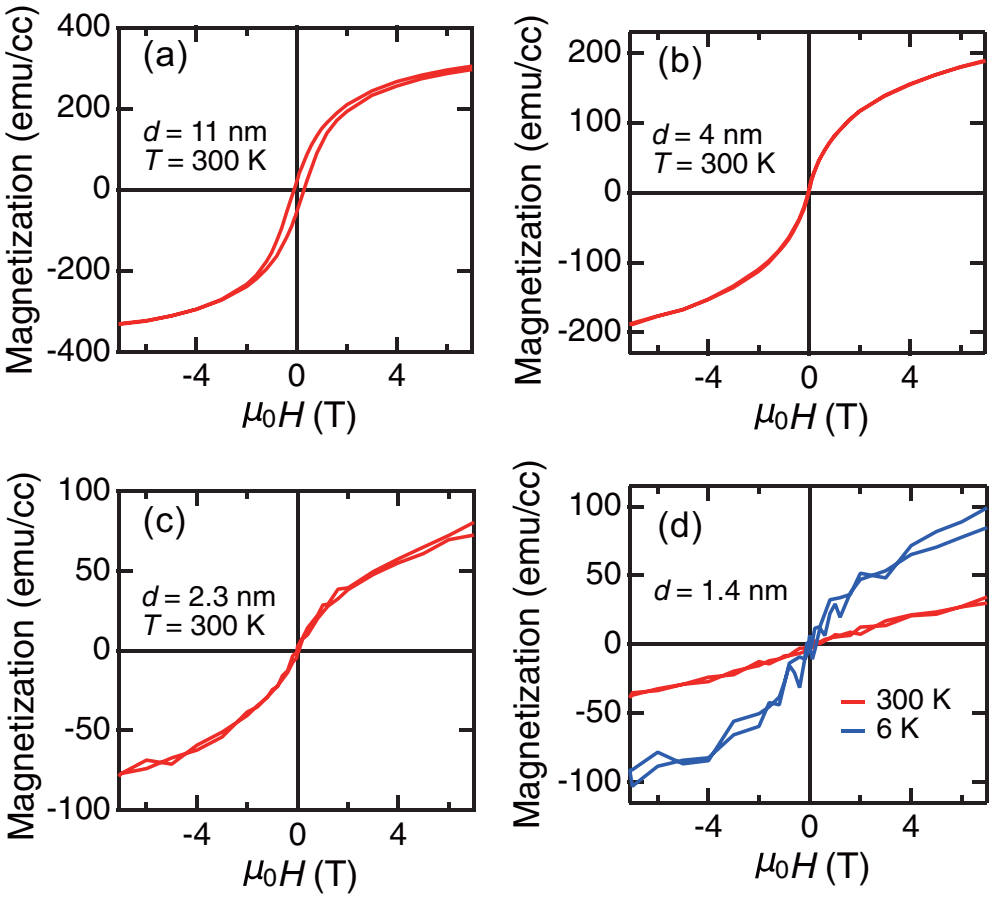

FIG. 10. XMCD-H curves measured at the Fe L_3 edge for the $CoFe_2O_4$ films with (a) $d = 11$ nm, (b) $d = 4$ nm, (c) $d = 2.3$ nm, and (d) $d = 1.4$ nm, in which red curves and blue curves represent the signals measured at 300 and 6 K, respectively. The vertical axis of the XMCD intensity has been scaled so that it represents the sum of the magnetizations of the Fe and Co cations estimated from the fits in Figs. 7(c), 7(d), 9(c), and 9(d).

larger but comparable to that in the Fe_3O_4 films. Furthermore, the absolute value of the slope of the magnetization d curve (Fig. 11) of the $CoFe_2O_4$ films in the small thickness range of 4 to 1.4 nm (58 emu/cc·nm) is significantly larger than that in the large thickness range of 11 to 4 nm (20 emu/cc · nm). The APBs model described above may indeed be applied in the large thickness range (11 to 4 nm), but it cannot be applied in the small thickness range (4 to 1.4 nm), since the decrease ratio in the large thickness range is comparable to the value reported for the Fe_3O_4 films, but the decrease ratio in the small thickness range is significantly larger than that in the large thickness range. In our samples, the density of the APBs does not clearly depend on the thickness of the $CoFe_2O_4$ layer from the cross-sectional TEM image in Fig. 4(b), whereas the cation distribution and electronic structure drastically change in the thickness range of 4 to 1.4 nm as shown in Fig. 8. Therefore, it is reasonable to conclude that the cation distribution and electronic structure predominantly affect the magnetic order in the $CoFe_2O_4$ region very close to the $CoFe_2O_4/Al_2O_3$ interface (within 4 nm). In future studies, it is also important to investigate the effect of the strain, intermixing, and oxygen deficiency/excess near the interface.

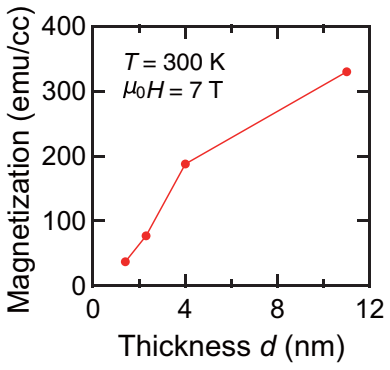

FIG. 11. Thickness (d) dependence of the sum of the magnetizations of the Fe and Co cations derived from the values of red curves at 7 T in Fig. 10.

IV. CONCLUSIONS

We have investigated the electronic structure and magnetic properties of the $CoFe_2O_4(111)$ layers with various thicknesses ($d = 1.4$, 2.3, 4, and 11 nm) in the epitaxial $CoFe_2O_4/Al_2O_3/Si$ structures. The XAS and XMCD spectra revealed that the magnetization gradually decreases with decreasing d, and finally, the magnetically dead layer was clearly detected at $d = 1.4$ nm. The magnetically dead layer has frustration of magnetic interactions, which was characterized

by the comparison of magnetizations measured at 300 and 6 K. Using these experimental XAS and XMCD spectra, the sites and valences of Fe cations were estimated by employing the CI cluster model. We found that the decrease of d leads to the decreases in the inverse-to-normal spinel structure ratio and in the average valence of the Fe cations at the O_h sites. These structural and chemical defects in a few nanometers thick $CoFe_2O_4$ layer will lead to the formation of unwanted midgap impurity states which decrease the efficiency of the spin filter effect [6,7,13]. From the experimental results and calculation, it was found that the magnetically dead layer at the $CoFe_2O_4/Al_2O_3$ interface probably originates from various complex networks of superexchange interactions through the change in the cation distribution and electronic structure. Furthermore, we have also found that the ferrimagnetic order of the magnetically dead layer at the $CoFe_2O_4/Al_2O_3$ interface is partially restored by increasing the thickness from $d = 1.4$ to 2.3 nm. These findings are important for the design of Si-based spintronic devices using spinel ferrites. To realize a highly efficient spin injection into Si by the spin filter effect through thin film spinel ferrites, interface engineering is strongly needed to control the cation distribution and electronic structure for a robust ferrimagnetic order and exclusion of midgap impurity states.

ACKNOWLEDGMENTS

The authors thank Mr. N. Uchida (The Univ. of Tokyo) for his help with the growth and crystalline characterization of the samples. This paper was partly supported by Grants-in-Aid for Scientific Research (Grants No. 26289086, No. 15H02109, and No. 15K17696), including the Project for Developing Innovation Systems from Ministry of Education, Culture, Sports, Science and Technology (MEXT), the Cooperative Research Project Program of Research Institute of Electrical Communication (RIEC), Tohoku University, and the Spintronics Research Network of Japan (SRNJ). The work in this paper was performed under the Shared Use Program of Japan Atomic Energy Agency (JAEA) Facilities (Proposal No. 2016A-E27) with the approval of the Nanotechnology Platform Project supported by MEXT (Proposal No. A-16-AE-0011). The synchrotron radiation experiments were performed at the JAEA beamline BL23SU in SPring-8 (Proposal No. 2016A3831). Y.K.W. and Z.C. acknowledge financial support from Japan Society for the Promotion of Science (JSPS) through the Program for Leading Graduate Schools (MERIT). S.S. acknowledges financial support from JSPS through the Program for Leading Graduate Schools (ALPS). Y.K.W. and S.S. also acknowledge support from the JSPS Research Fellowship Program for Young Scientists.

[1] S. Sugahara and M. Tanaka, Appl. Phys. Lett. **84**, 2307 (2004).
[2] T. Tahara, H. Koike, M. Kameno, T. Sasaki, Y. Ando, K. Tanaka, S. Miwa, Y. Suzuki, and M. Shiraishi, Appl. Phys. Express **8**, 113004 (2015).
[3] R. Nakane, T. Harada, K. Sugiura, and M. Tanaka, Jpn. J. Appl. Phys. **49**, 113001 (2010).
[4] R. Bachelet, P. de Coux, B. Warot-Fonrose, V. Skumryev, G. Niu, B. Vilquin, G. Saint-Girons, and F. Sánchez, Cryst. Eng. Commun. **16**, 10741 (2014).
[5] Y. Suzuki, R. B. van Dover, E. M. Gyorgy, J. M. Phillips, V. Korenivski, D. J. Werder, C. H. Chen, R. J. Cava, J. J. Krajewski, W. F. Peck, Jr., and K. B. Do, Appl. Phys. Lett. **68**, 714 (1996).
[6] A. V. Ramos, M.-J. Guitted, J.-B. Moussy, R. Mattana, C. Deranlot, F. Petroff, and C. Gatel, Appl. Phys. Lett. **91**, 122107 (2007).
[7] Z. Szotek, W. M. Temmerman, D. Kodderitzsch, A. Svane, L. Petit, and H. Winter, Phys. Rev. B **74**, 174431 (2006).
[8] J. S. Moodera, T. S. Samtos, and T. Nagahama, J. Phys.: Condens. Matter **19**, 165202 (2007).
[9] J-B. Moussy, J. Phys. D: Appl. Phys. **46**, 143001 (2013).
[10] F. C. Voogt, T. T. M. Palstra, L. Niesen, O. C. Rogojanu, M. A. James, and T. Hibma, Phys. Rev. B **57**, R8107 (1998).
[11] D. T. Margulies, F. T. Parker, M. L. Rudee, F. E. Spada, J. N. Chapman, P. R. Aitchison, and A. E. Berkowitz, Phys. Rev. Lett **79**, 5162 (1997).
[12] J.-B. Moussy, S. Gota, A. Bataille, M.-J. Guittet, M. Gautier-Soyer, F. Delille, B. Dieny, F. Ott, T. D. Doan, P. Warin, P. Bayle-Guillemaud, C. Gatel, and E. Snoeck, Phys. Rev. B **70**, 174448 (2004).
[13] Y. K. Takahashi, S. Kasai, T. Furubayashi, S. Mitani, K. Inomata, and K. Hono, Appl. Phys. Lett. **96**, 072512 (2010).
[14] T. Niizeki, Y. Utsumi, R. Aoyama, H. Yanagihara, J. -I. Inoue, Y. Yamasaki, H. Nakao, K. Koike, and E. Kita, Appl. Phys. Lett. **103**, 162407 (2013).
[15] B. T. Thole, P. Carra, F. Sette, and G. van der Laan, Phys. Rev. Lett. **68**, 1943 (1992).
[16] C. T. Chen, Y. U. Idzerda, H. -J. Lin, N. V. Smith, G. Meigs, E. Chaban, G. H. Ho, E. Pellegrin, and F. Sette, Phys. Rev. Lett. **75**, 152 (1995).
[17] J. Stohr and H. Konig, Phys. Rev. Lett. **75**, 3748 (1995).
[18] Y. K. Wakabayashi, S. Sakamoto, Y. Takeda, K. Ishigami, Y. Takahashi, Y. Saitoh, H. Yamagami, A. Fujimori, M. Tanaka, and S. Ohya, Sci. Rep. **6**, 23295 (2016).
[19] Y. K. Wakabayashi, R. Akiyama, Y. Takeda, M. Horio, G. Shibata, S. Sakamoto, Y. Ban, Y. Saitoh, H. Yamagami, A. Fujimori, M. Tanaka, and S. Ohya, Phys. Rev. B **95**, 014417 (2017).
[20] S. Matzen, J.-B. Moussy, R. Mattana, F. Petroff, C. Gatel, B. Warot-Fonrose, J. C. Cezar, A. Barbier, M.-A. Arrio, and Ph. Sainctavit, Appl. Phys. Lett. **99**, 052514 (2011).
[21] S. Matzen, J.-B. Moussy, R. Mattana, K. Bouzehouane, C. Deranlot, F. Petroff, J. C. Cezar, M.-A. Arrio, Ph. Sainctavit, C. Gatel, B. Warot-Fonrose, and Y. Zheng, Phys. Rev. B **83**, 184402 (2011).
[22] B. B. Nelson-Cheeseman, R. V. Chopdekar, J. M. Iwata, M. F. Toney, E. Arenholz, and Y. Suzuki, Phys. Rev. B **82**, 144419 (2010).
[23] A. Tanaka and T. Jo, J. Phys. Soc. Jpn. **63**, 2788 (1994).
[24] D. J. Hnatowich, J. Hudis, M. L. Perlman, and R. C. Ragaini, J. Appl. Phys. **42**, 4883 (1971).
[25] Y. Jung, H. Miura, and M. Ishida, Jpn. J. Appl. Phys. **38**, 2333 (1999).

[26] See Supplemental Material at http://link.aps.org/supplemental/10.1103/PhysRevB.96.104410 for the LEED and XRD measurements, XAS and XMCD spectra with the thickness $d = 1.4$, 2.3, and 4 nm, XMCD-$\mu_0 H$ curves measured at the Fe and Co L_3 edges, and the thickness (d) dependence of the maximum XAS intensity at the Fe L_3 edge.

[27] W. Eerenstein, T. T. M. Palstra, T. Hibma, and S. Celotto, Phys. Rev. B **66**, 201101(R) (2002).

[28] Y. Saitoh, Y. Fukuda, Y. Takeda, H. Yamagami, S. Takahashi, Y. Asano, T. Hara, K. Shirasawa, M. Takeuchi, T. Tanaka, and H. Kitamura, J. Synchrotron Rad. **19**, 388 (2012).

[29] R. Nakajima, J. Stohr, and Y. U. Idzerda, Phys. Rev. B **59**, 6421 (1999).

[30] J. Chen, D. J. Huang, A. Tanaka, C. F. Chang, S. C. Chung, W. B. Wu, and C. T. Chen, Phys. Rev. B **69**, 085107 (2004).

[31] Y. Fukuma, T. Taya, S. Miyawaki, T. Irisa, H. Asada, and T. Koyanagi, J. Appl. Phys. **99**, 08D508 (2006).

[32] M. Oku and K. Hirokawa, J. Electron Spectrosc. Relat. Phenom. **8**, 475 (1976).

[33] S. Niitaka, H. Kageyama, M. Kato, K. Yoshimura, and K. Kosuge, J. Solid State Chem. **146**, 137 (1999).

[34] C. F. Chang, Z. Hu, S. Klein, X. H. Liu, R. Sutarto, A. Tanaka, J. C. Cezar, N. B. Brookes, H.-J. Lin, H. H. Hsieh, C. T. Chen, A. D. Rata, and L. H. Tjeng, Phys. Rev. X **6**, 041011 (2016).